Supporting information

Template-free Synthesis of Yolk-Shell Co_3O_4/Nitrogen-Doped Carbon Microstructure for Excellent Lithium Ion Storage

Ming-Jun Xiao,[a] Hong Zhang,[b] Bo Ma,[a] Ze-Qi Zhang,[a] Xiang Yang Li,[a] Qi Xiao,[a] Qiang Wang,*[a] Yong Peng,*[b] and Hao-Li Zhang*[a c]

a State Key Laboratory of Applied Organic Chemistry, Key Laboratory of Special Function Materials and Structure Design, College of Chemistry and Chemical Engineering, Lanzhou University, Lanzhou, 730000, P. R. China.

b Key Laboratory of Magnetism and Magnetic Materials of MOE, Lanzhou University, Lanzhou, 730000, P. R. China.

c Tianjin Key Laboratory of Molecular Optoelectronic Sciences, Department of Chemistry, Tianjin University, Collaborative Innovation Center of Chemical Science and Engineering (Tianjin), Tianjin 300072, P. R. China.

*Corresponding author.

E-mail: haoli.zhang@lzu.edu.cn, qiangwang@lzu.edu.cn, pengy@lzu.edu.cn

Simulations of atomic resolution STEM images

The quantitative simulations of the atomic resolution STEM images were carried out by using quantitative TEM/STEM Simulations Package (QSTEM, Arizona State University, USA). The simulation parameters were set up as the same as possible to the experimental conditions. The high voltage, Cs coefficient, Cc coefficients and defocus were 300 kV, 50 μm, 1.2 mm and 0 nm, respectively. The unit cells of Nx, Ny and Nz were set to be 8 × 8 × 10 for slab calculations. The inner angle and outer angle of HAADF detectors were 90 mrad and 170 mrad. The semi-angle of the incident converged beam was set to be 20 mrad. All simulated images were used the same thickness, 82.7 Å, which came from the TEM measured data. Thermal Diffuse Scattering (TDS) runs has been set up 30.

Computational method

The spin-unrestricted density functional theory (DFT) calculations were carried out by using a Dmol^3 package. Exchange-correlation functions are taken as generalized gradient approximation (GGA) with Perdew-Burke-Ernzerhof (PBE). DFT semicorepseudopotentials (DSPPs) core treatment was implemented for relativistic effects, which replaced core electrons by a single effective potential. Double numerical plus polarization (DNP) was employed as the basis set. The convergence tolerance of energy of 10^{-8} hartree was taken (1 hartree = 27.21 eV), and the maximal allowed force and displacement were 0.002 hartree Å^{-1} and 0.005 Å, respectively. In the simulation, three-dimensional periodic boundary conditions were taken. The simulation cell consisted of a Co_3O_4 super-cell. All atoms were allowed to relax according to previous reports. After structure relaxations, the band structure was calculated with high precision. Brillouin zone was sampled by G-centered meshes with fine k-points for the system. A vacuum layer of at least 20 Å was adopted in the direction perpendicular to the surface to avoid the interactions between periodic slabs. We employed the CI-neb method to calculate the energy barrier and locate transition states during the cross processes of lithium atom from the Co_3O_4/carbon boundary and from Co_3O_4, respectively[1].

Equivalent circuit model of Nyquist plots

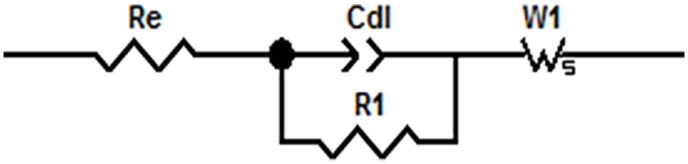

Re represents the intrinsic resistance, *R1* represents the electrode and electrolyte interface charge transfer impedance, *Cdl* denotes the double-layer capacitance, and *W1* denotes the Warburg impedance[2].

Lithium ion diffusion coefficient (D_{Li+}) calculation

The diffusion coefficient of lithium ion (D_{Li+}) of the electrode reaction can be calculated by using the following equations, respectively[3, 4]:

$$D_{Li^+} = \frac{R^2T^2}{2A^2n^4F^4C^2\sigma_W^2} \quad \text{(S1)}$$

where R is gas constant, T is the absolute temperature (298 K), A is electrode surface area ($A=1.13\times10^{-4}$ m^2), n is the number of electrons transferred (n=8), F is Faraday constant, C is Li^+ phase concentration, and σ_w is Warburg coefficient. The σ_w can be calculated by using the following Eq.[5, 6]:

$$Z^{'} = R_{e} + R_{ct} + \sigma_{w}\omega^{-0.5} \tag{S2}$$

The w is the angular frequency. Thus, σ_w can be obtained by linear fitting Z' vs. $w^{-0.5}$ the low-frequency range. For the exchange current density, it is only necessary to substitute the parameters of equivalent circuit parameters that have been fitted in the electrochemical impedance spectroscopy (EIS) into the Eq. (1). The calculated lithium diffusion coefficient of open yolk-shell Co_3O_4/NDC is 3.446×10^{-16} cm^2 s^{-1}, however that of open yolk-shell Co_3O_4 is 1.068×10^{-16} cm^2 s^{-1}, respectively.

Table S1. EIS Fitted results of open yolk-shell Co_3O_4/NDC and open yolk-shell Co_3O_4.

Sample	Equivalent series resistance (Re)	Charge transfer resistance (R1)	Li^+ diffusion coefficient (D_{Li+})
Open yolk-shell Co_3O_4/NDC	8.61 Ω	142 Ω	3.44×10^{-16} cm^2 s^{-1}
Open yolk-shell Co_3O_4	9.21 Ω	318 Ω	1.068×10^{-16} cm^2 s^{-1}

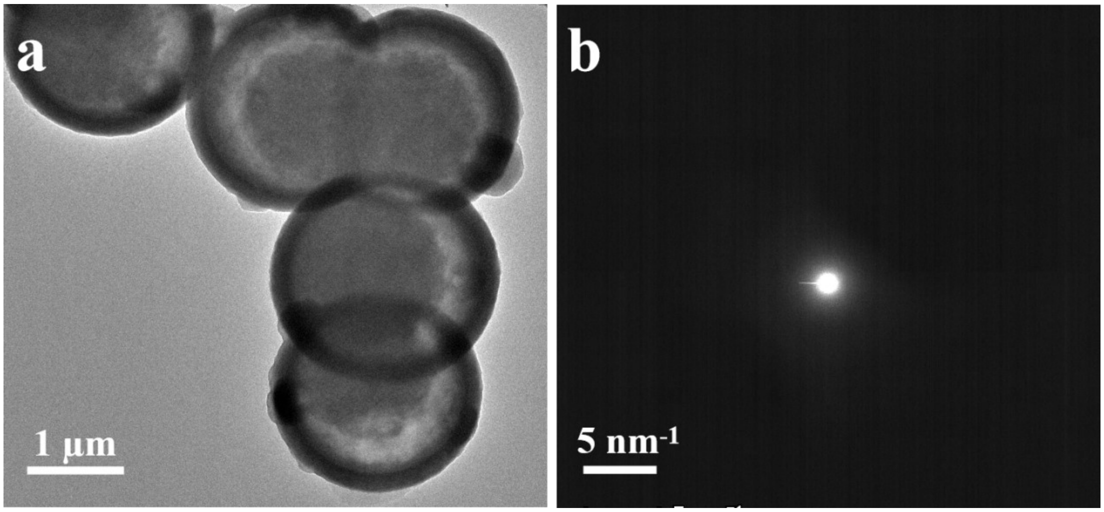

Fig. S1. The TEM image (a) and the selected area electron diffraction (SAED) patterns (b) of open yolk-shell amCoC.

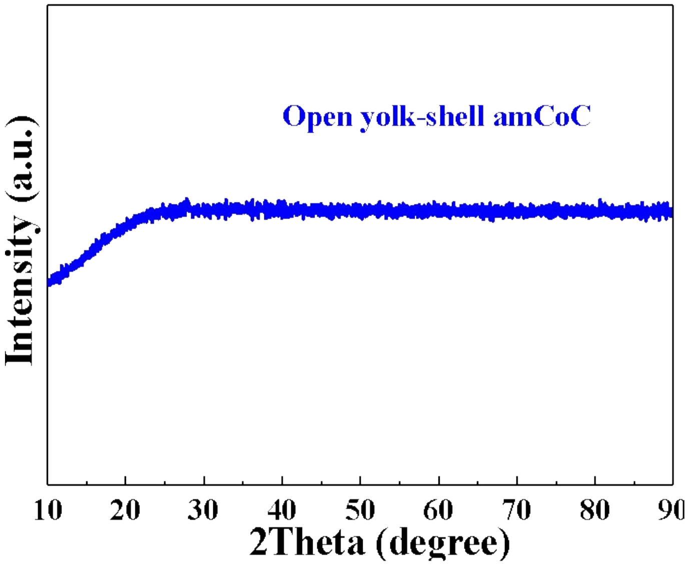

Fig. S2. XRD pattern of open yolk-shell amCoC.

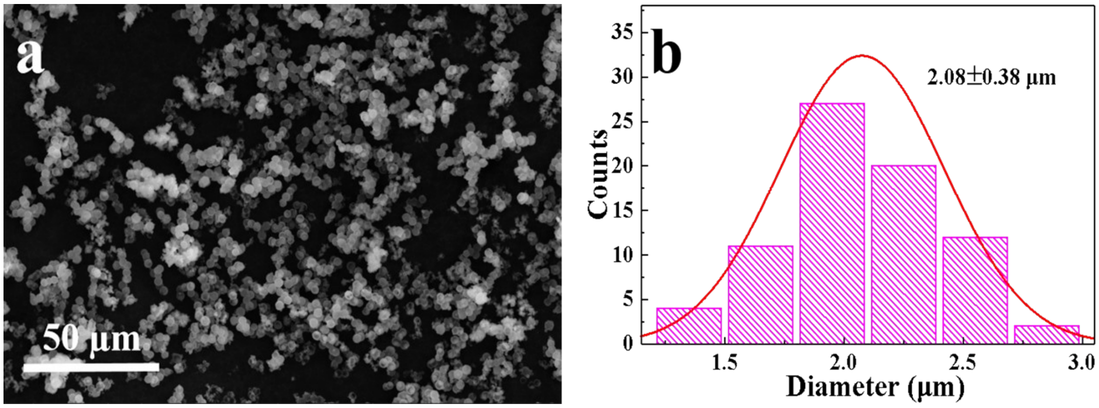

Fig. S3. SEM image (a) and the corresponding particle size statistics (b) of open yolk-shell amCoC.

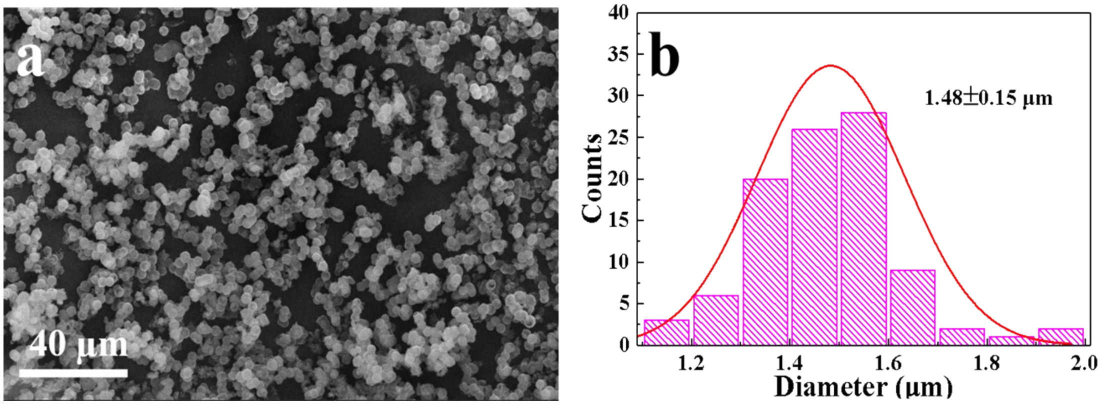

Fig. S4. SEM image (a) and the corresponding particles size statistics (b) of open yolk-shell Co_3O_4/NDC.

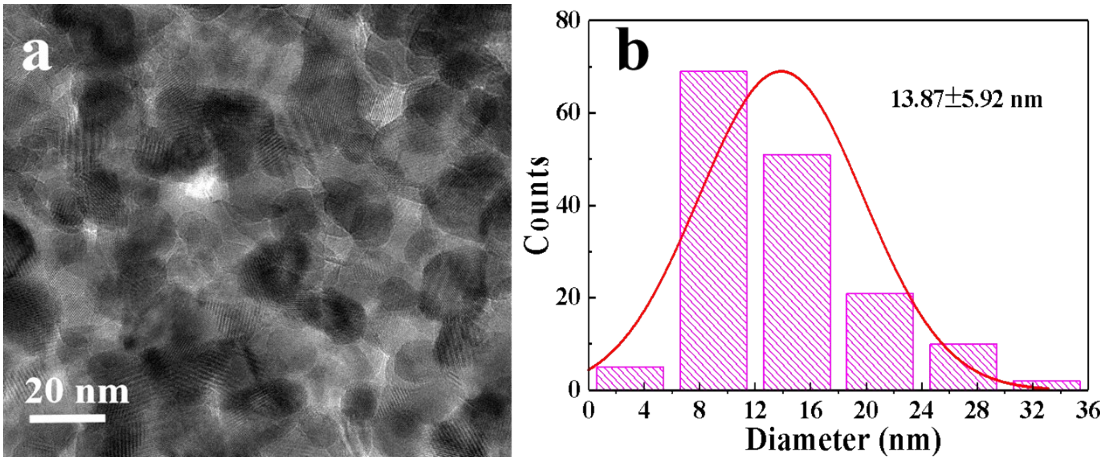

Fig. S5. TEM image (a) and the corresponding particle size statistics (b) of Co_3O_4/NDC.

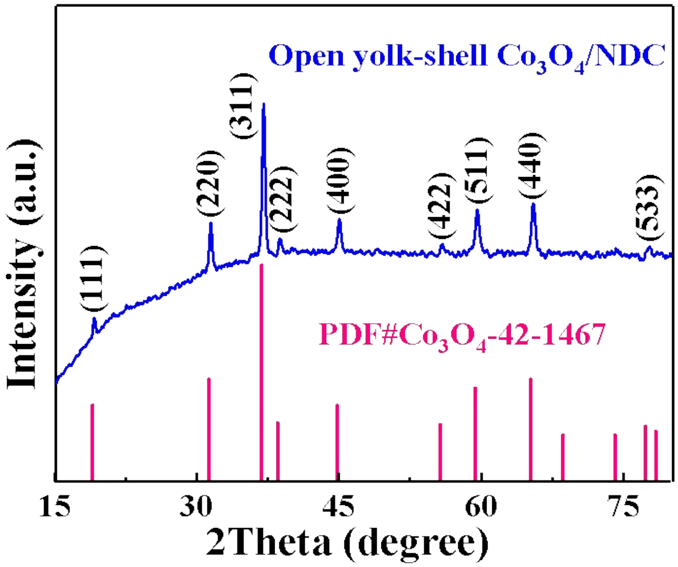

Fig. S6. XRD pattern of open yolk-shell Co_3O_4/NDC.

The XRD patterns of the open yolk-shell Co_3O_4/NDC matches well with the standard card of Co_3O_4 (PDF#Co_3O_4-42-1467)[7]. There are no distinguishable peaks of other cobalt oxides in the XRD, indicating that the prepared Co_3O_4 is relatively pure. No carbon peaks were observed due to their low content. It was proved that Co_3O_4 were successfully prepared. The grain size of the Co_3O_4 can be estimated from the broadening of XRD diffraction peaks according to the Scherrer equation: $D = \frac{K\lambda}{\beta\cos\theta}$, where D is the grain size, K is the Scherrer constant (0.89), b is the full width at half maximum obtained from XRD spectra and θ is the diffraction angle[8]. The grain sizes open yolk-shell Co_3O_4/NDC estimated to be around 13.2 nm based on the strongest diffraction peak from the (311) crystal plane.

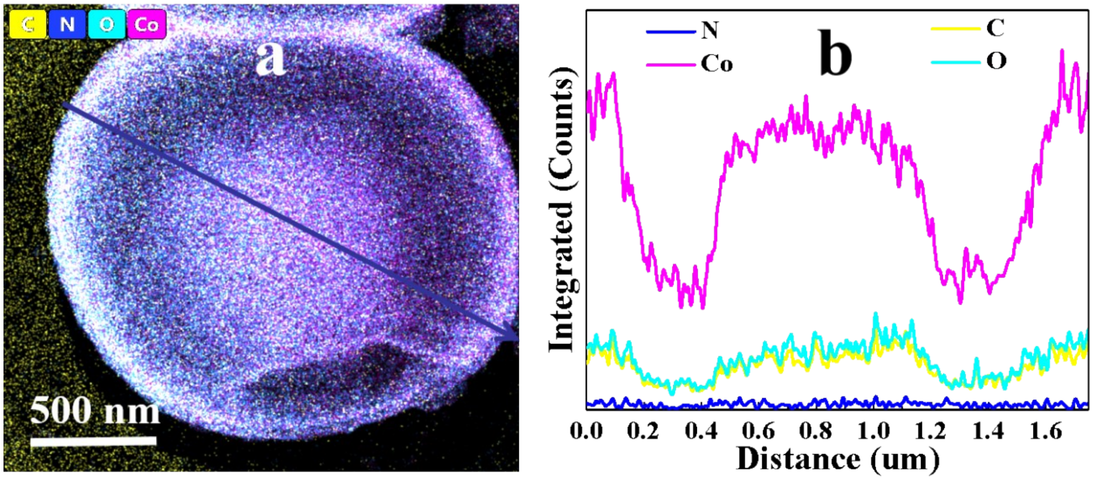

Fig. S7. The element mapping and corresponding line scanning of Co, O, C, and N in open yolk-shell Co_3O_4/NDC.

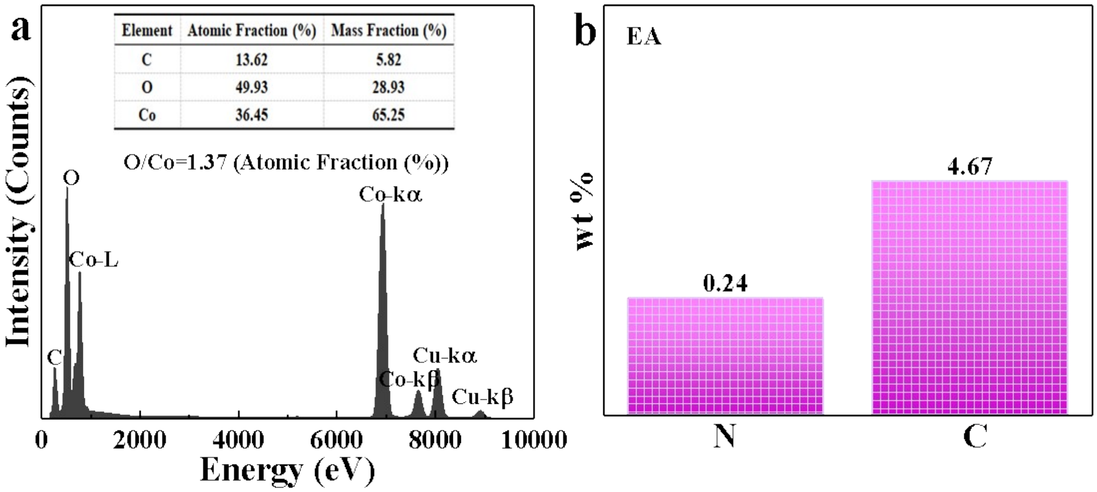

Element	Atomic Fraction (%)	Mass Fraction (%)
C	13.62	5.82
O	49.93	28.93
Co	36.45	65.25

O/Co=1.37 (Atomic Fraction (%))

Fig. S8. The energy dispersive spectroscopy (EDS) (a) and elemental analysis (b) of open yolk-shell Co_3O_4/NDC.

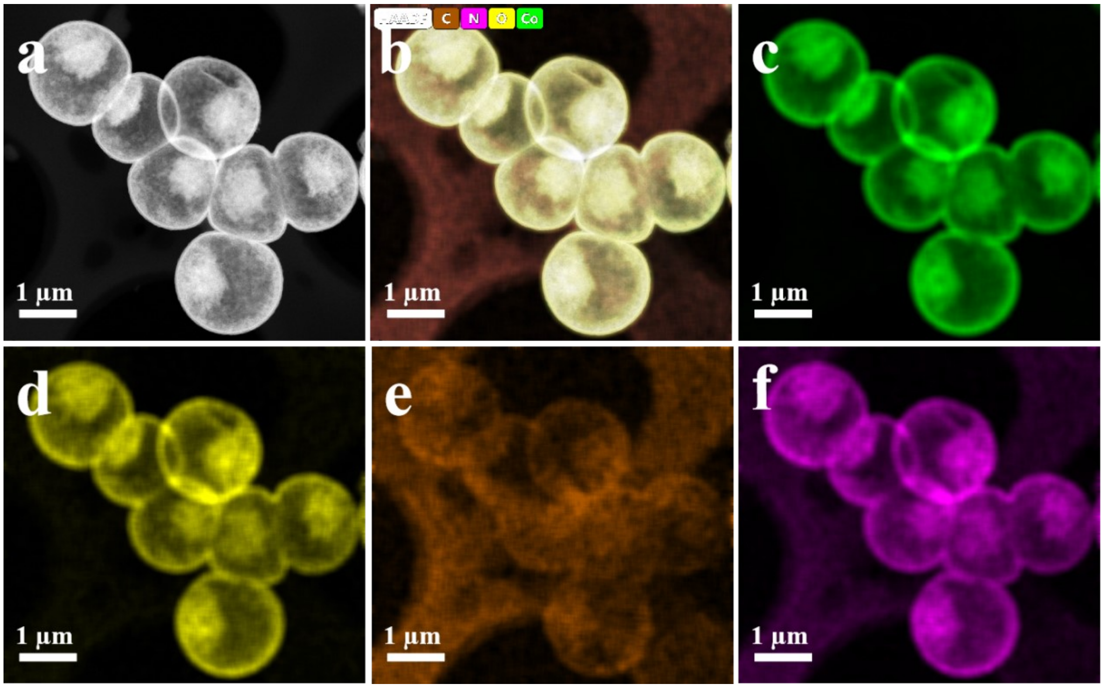

Fig. S9. High-angle annular dark-field **(**HAADF)-STEM image (a) and element mapping (b-f) of open yolk-shell Co_3O_4/NDC.

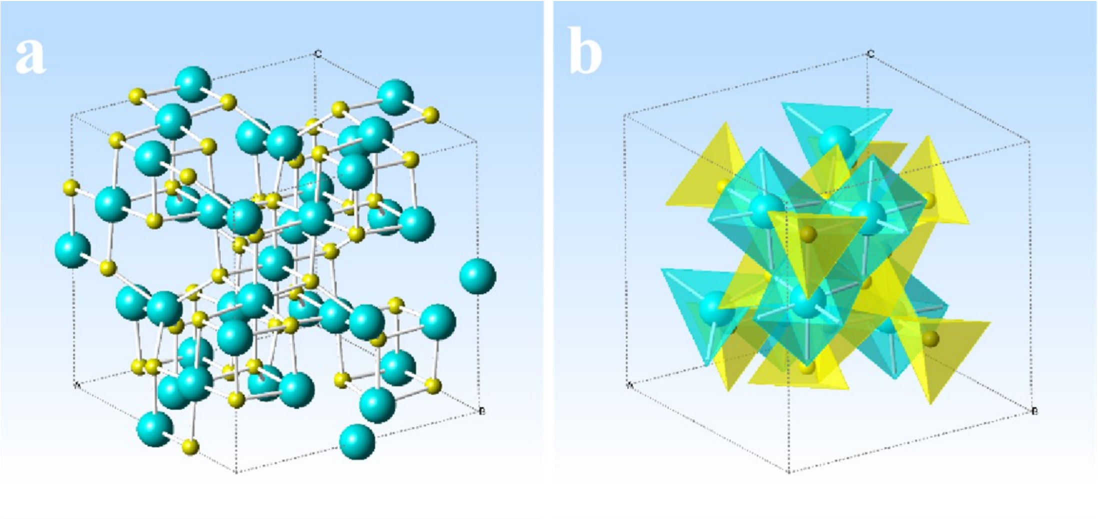

Fig. S10. Crystal structure of spinel Co_3O_4: (a) single cell "ball-and-stick" model, (b) polyhedron model.

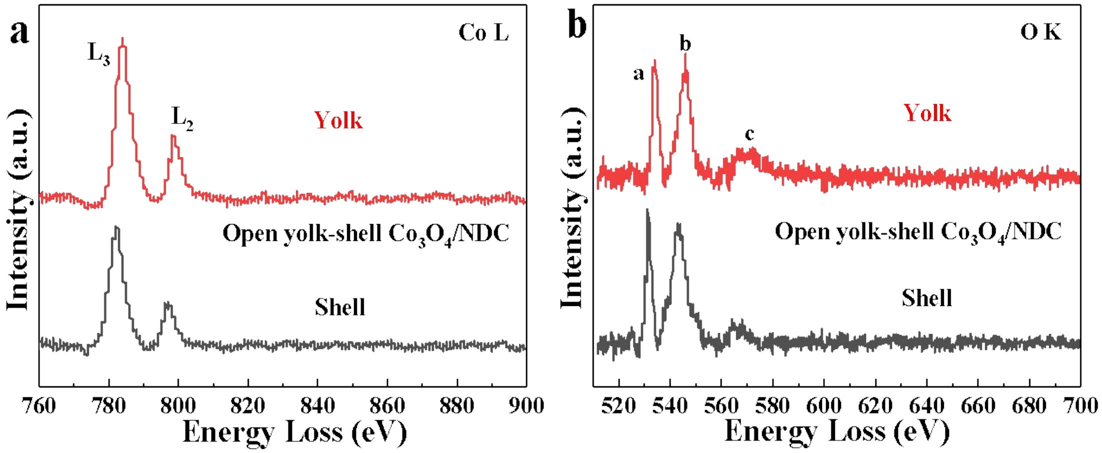

Fig. S11. Electron energy loss spectroscopy (EELS) spectra of Co L-edge (d) and O k-edge (e) at yolk and shell of open yolk-shell Co_3O_4/NDC.

The EELS analyses on the open yolk-shell Co_3O_4/NDC was performed on the STEM. **Fig. S11a-b** shows the EELS spectra at Co L- and O K-edges from the yolk and shell of the open yolk-shell Co_3O_4/NDC. For the Co L-edge spectra of yolk and shell, no noticeable changes in the L_3/L_2 ratio are found, suggesting that the oxidation state of Co ion remain unchanged[9, 10]. For the O K-edge spectra of yolk and shell, three characteristic peaks near the edge onset labeled a, b, and c, are observed. The a, b and c are assigned to the hybridization of O 2p with Co 3d, Co 5d, and Co 4sp orbitals, Respectively. Compared with that from the center position, the spectrum from the edge shows an obvious reduction in the intensity. This reduction is generally attributed to the weakening of Co 3d-O 2p hybridization[10].

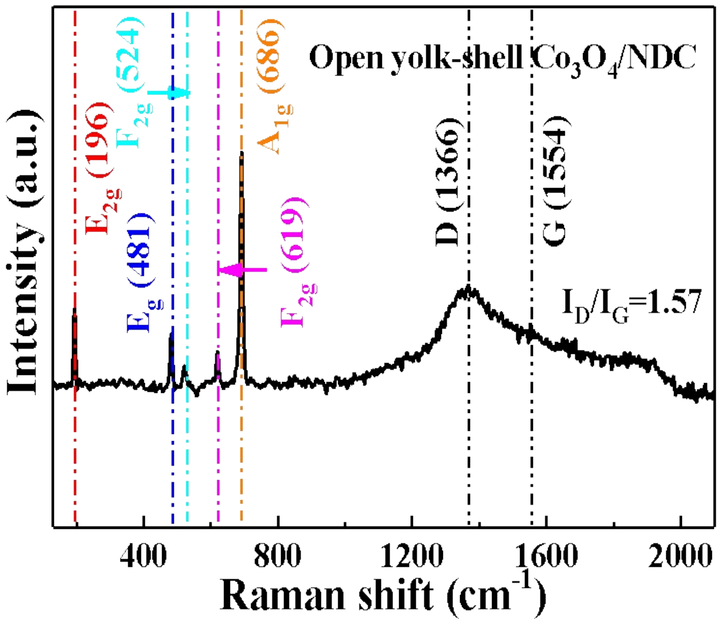

Fig. S12. The Raman spectrum of the open yolk-shell Co_3O_4/NDC.

The peaks of 195 cm^{-1}, 479 cm^{-1}, 521 cm^{-1}, 617 cm^{-1}, and 685 cm^{-1} in the Raman spectrum of open yolk-shell Co_3O_4/NDC correspond to F_{2g}, E_g, F_{12g}, F_{22g}, and A_{1g} vibration modes of Co_3O_4, respectively[11]. The carbon in the open yolk-shell Co_3O_4/NDC has two obvious vibration peaks at 1366 cm^{-1} and 1554 cm^{-1}, namely A_{1g} vibration (D band) and E_{2g} vibration (G band) modes. The D band corresponds to disordered carbon (sp^3) and defects, and the G band is related to ordered graphite carbon (sp^2)[12]. The peak intensity ratio (I_D/I_G) is a useful index to characterize the graphitic degree of carbon materials. The I_D/I_G value of the open yolk-shell Co_3O_4/NDC is about 1.57, indicated that the carbon in the open yolk-shell Co_3O_4/NDC has high degree of disorder[13].

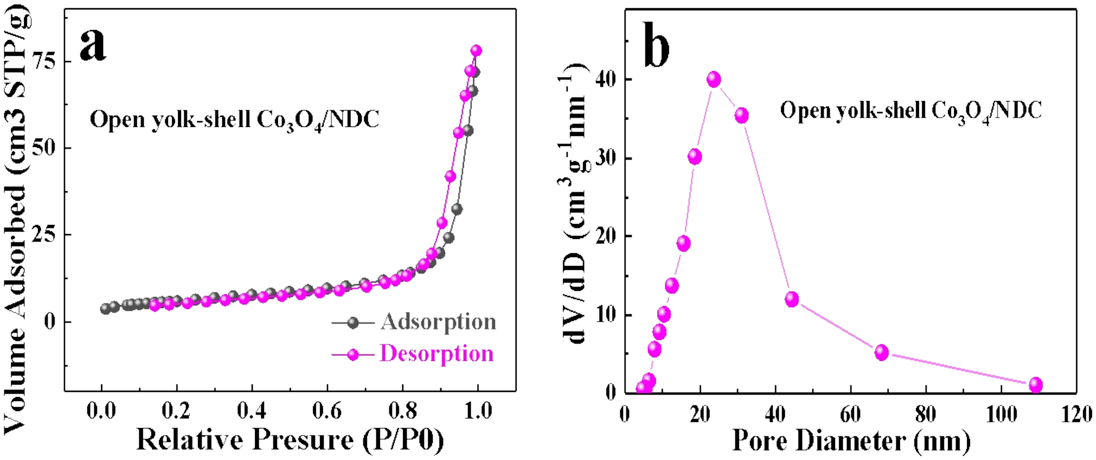

Fig. S13. BET (a) and the pore size distribution (b) of open yolk-shell Co_3O_4/NDC.

The nitrogen adsorption/desorption isotherms illustrate that open yolk-shell Co_3O_4/NDC possesses a large BET specific surface area of 21.485 m^2 g^{-1} (**Fig. S13a**). The Type I isotherms with the pronounced hysteresis loop and rapid nitrogen uptake at low-pressure region ($P/P_0 < 0.1$) were observed, suggest the existence of mesopores[14]. As shown in **Fig. S13b**, the mesopores (~25 nm) is observed. For lithium ion batteries, the mesopores can serve as channels for the rapid ion transport[15].

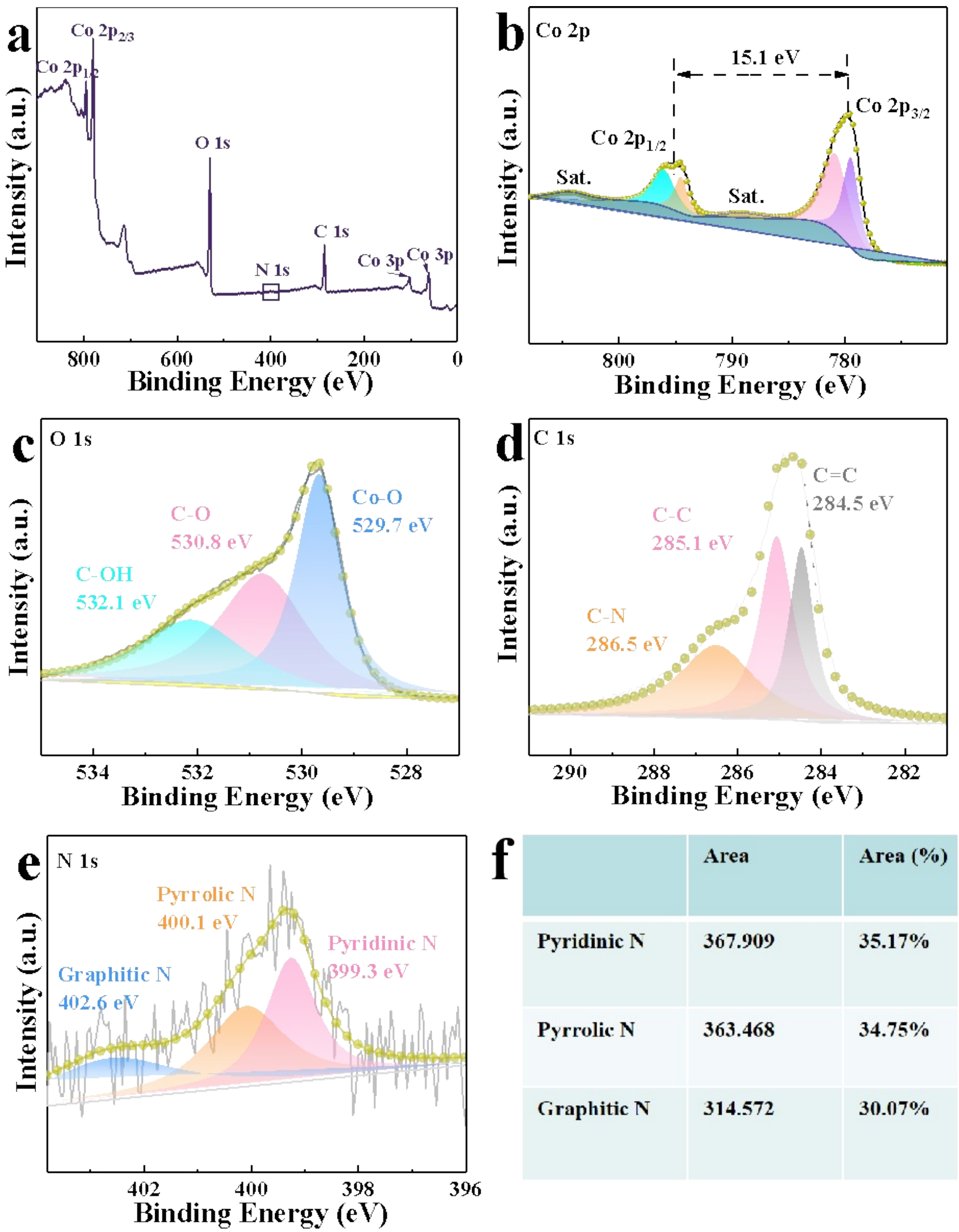

	Area	Area (%)
Pyridinic N	367.909	35.17%
Pyrrolic N	363.468	34.75%
Graphitic N	314.572	30.07%

Fig. S14. XPS survey (a) and high-resolution of Co 2p (b), O 1s (c), C 1s (d), N 1s (e), and the content of different type nitrogen (f) of open yolk-shell Co_3O_4/NDC.

The XPS spectra analysis shows four characteristic peaks located at 779.8 eV, 529.8 eV, 284.8 eV, and 400.2 eV, corresponding to the Co 2p, O 1s, C 1s, and N 1s, respectively (**Fig. S14a**). To further identify the states of Co, O, C, and N, we fitted Co 2p, O 1s, C 1s, and N 1s. **Fig. S14b** shows the XPS spectrum of Co 2p peaks. The binding energy of Co $2p_{1/2}$ and Co $2p_{3/2}$ are observed about 796.0 eV, 794.5 eV, 780.8 eV and 779.4 eV, and the distance between the two peaks is about 15.1 eV[16], indicating the coexistence of Co^{2+} and Co^{3+}. The O 1s spectrum (**Fig. S14c**) splits into three distinct peaks at 529.7 eV, 530.8 eV, and 532.1 eV, which can be assigned to the Co-O, C-O, and C-OH bonds, respectively[17]. The C-O bond can yield a C-O-Co bond that binds the carbon material to Co_3O_4. The C-OH bond indicates that the IL is not fully carbonized. The C 1s spectrum (**Fig. S14d**) splits into three peaks at 284.5 eV, 285.1 eV, and 286.5 eV, respectively. The peak of 284.5 eV and 285.1 eV corresponds to the C=C bond and C-C bond, respectively[18]. The peak at 286.5 eV, which is attributed to the C-N bond, indicates that nitrogen is successfully doped in the carbon material. The N 1s spectrum could be divided into four peaks with binding energy values of 399.3 eV, 400.1 eV, and 402.6 eV that correspond to pyridinic N, pyrrolic N, and graphitic N, respectively (**Fig. S14e**)[19]. According to the calculation of peak area, the nitrogen content is 0.2 wt.%, which is mainly pyridinic N (35.17%) and pyrrolic N (34.75%) (**Fig. S14f**). The pyridinic N and pyrrolic N can form defects, and are beneficial to enhance the surface wettability and provide a large number of active sites for lithium ion adsorption[20].

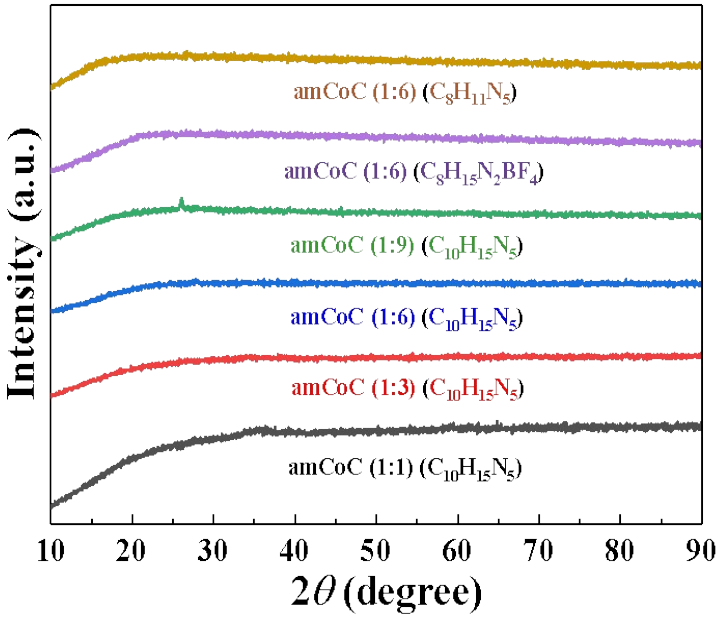

Fig. S15. XRD patterns of different morphology amCoC (Co:IL=1:1, 1:3, 1:6, 1:9).

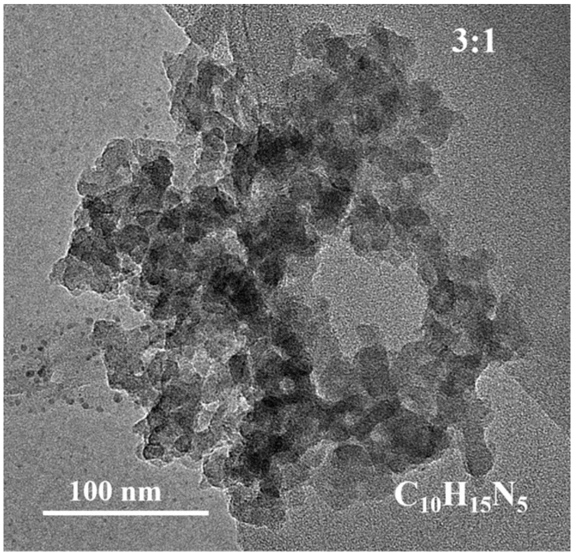

Fig. S16. TEM image of amCoC (Co:IL=3:1).

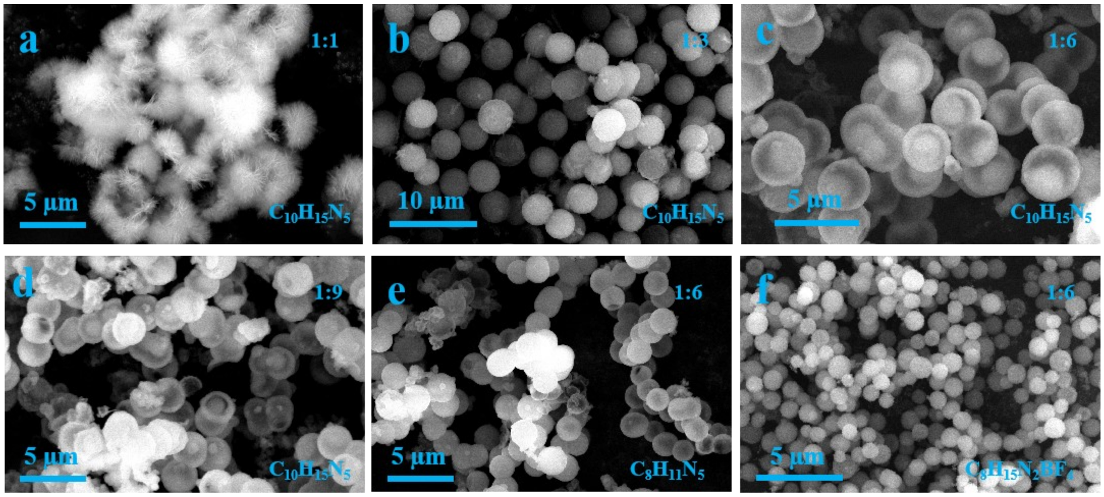

Fig. S17. SEM images (a-f) of different morphology amCoC (Co:IL=1:1, 1:3, 1:6, 1:9).

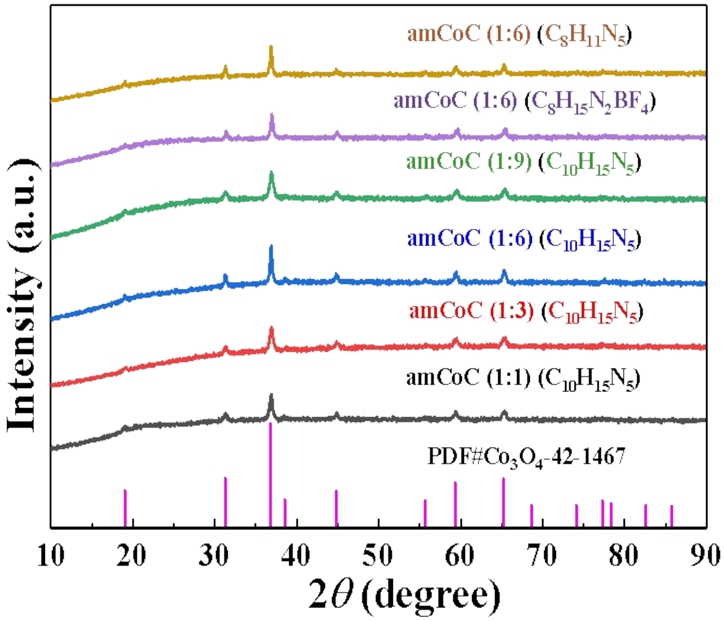

Fig. S18. XRD patterns of different morphology Co_3O_4/NDC (Co:IL=1:1, 1:3, 1:6, 1:9).

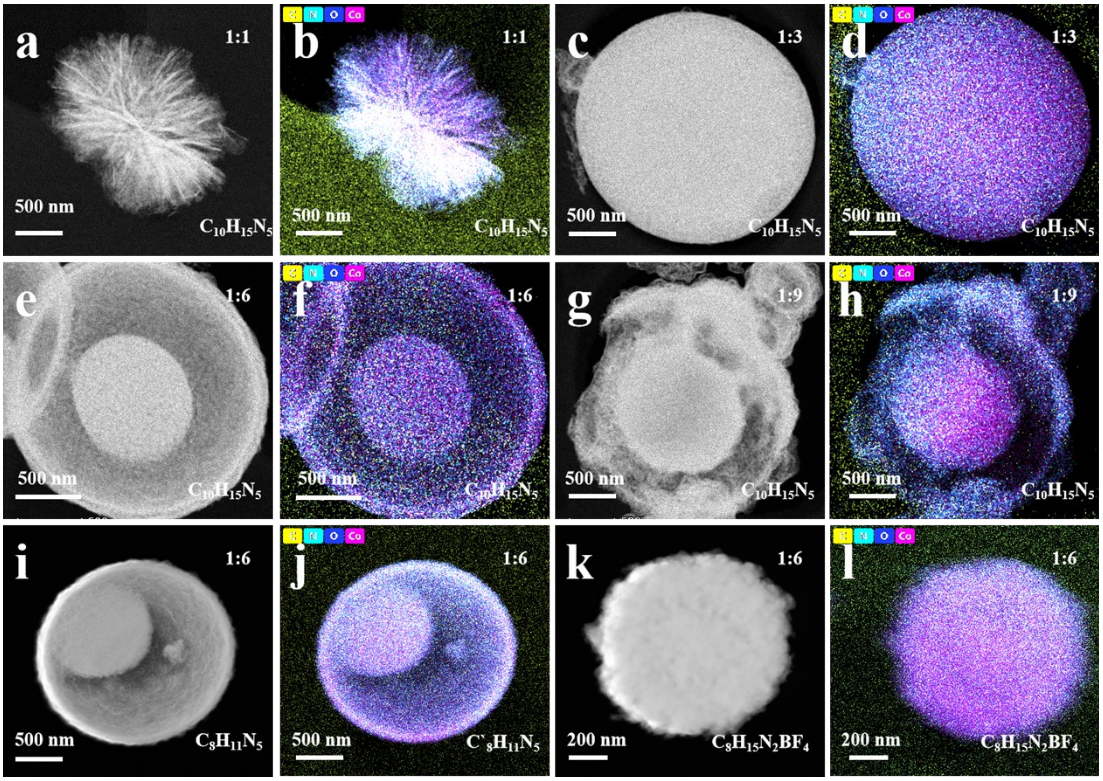

Fig. S19. HADDF-STEM images and element mapping (a-l) of different morphology Co_3O_4/NDC (Co:IL=1:1, 1:3, 1:6, 1:9).

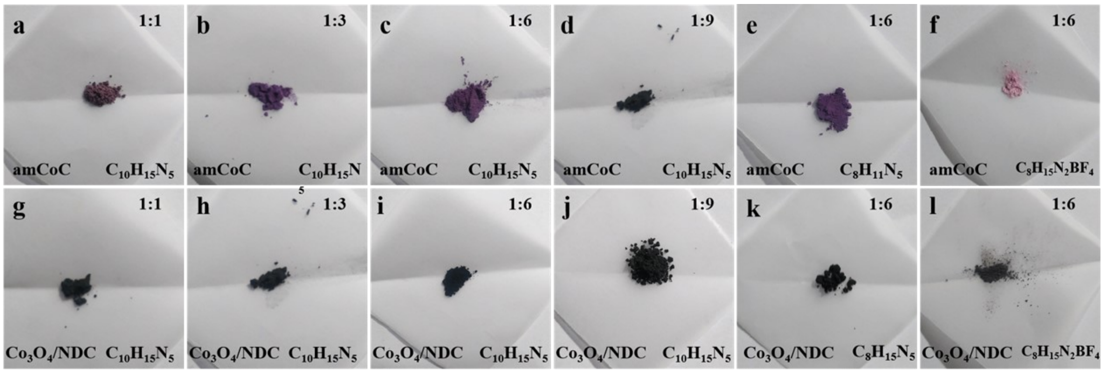

Fig. S20. The optical images from different morphology amCoC to different morphology Co_3O_4/NDC (Note: The powers of different materials are seen on weighting papers with a size of 5.6 cm x 5.2 cm).

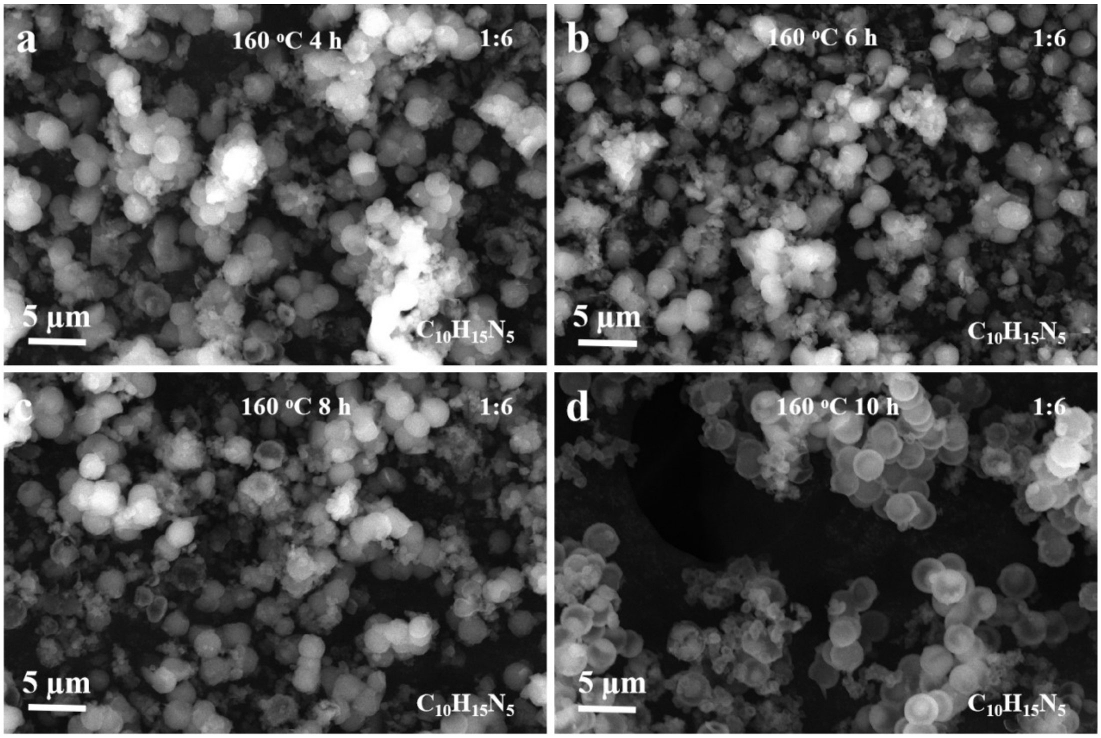

Fig. S21. SEM images of the amCoC at different reaction time at 160 °C in the high-pressure reactor (a-d) (Co:IL=1:6).

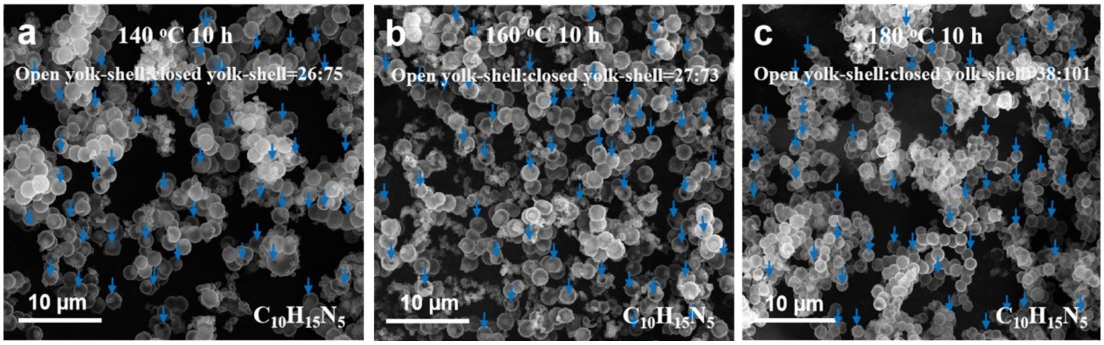

Fig. S22. SEM image and statistics on the number of open yolk-shell Co_3O_4/NDC at different reaction temperature in the high-pressure reactor (Co:IL=1:6).

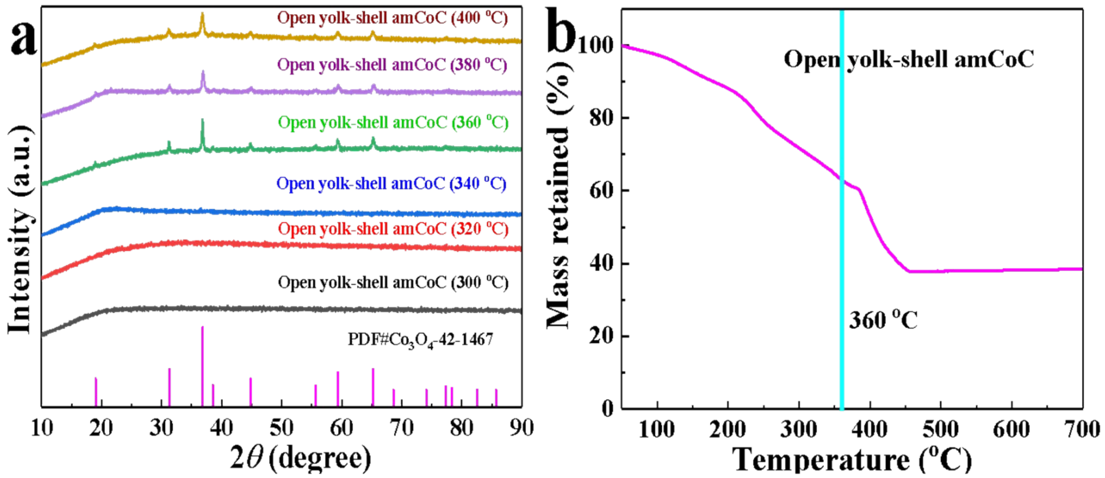

Fig. S23. The XRD of the open yolk-shell amCoC synthesized at different temperatures under air atmosphere (a). The Thermo-gravimetric (TG) curves of the open yolk-shell amCoC under air atmosphere, the sample was synthesized by heating treatment at 160 °C for 10 hours (b).

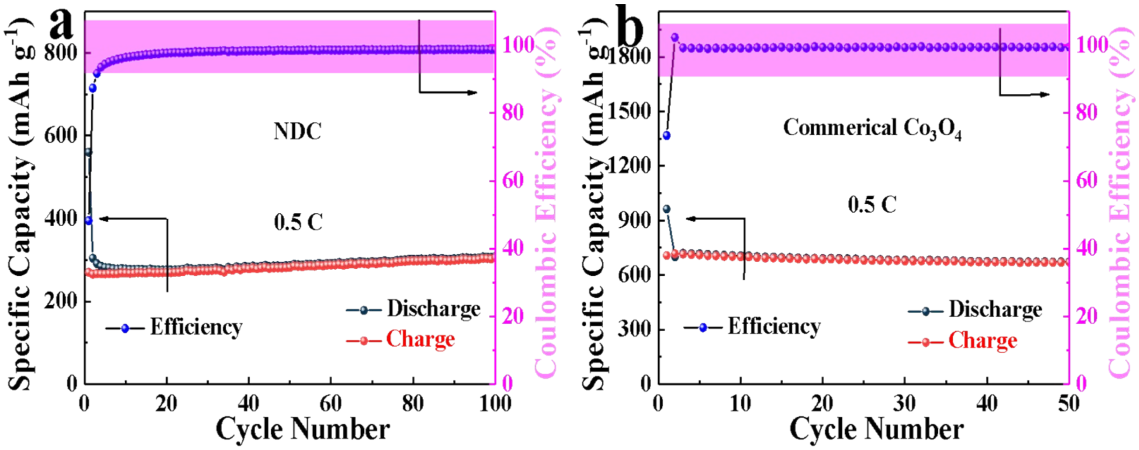

Fig. S24. Comparison of cycling performance of NDC (a) and commercial Co_3O_4 (Shanghai Macklin Biochemical Co.,Ltd, Metals basis of 99.99%) (b) at current density of 0.5 C.

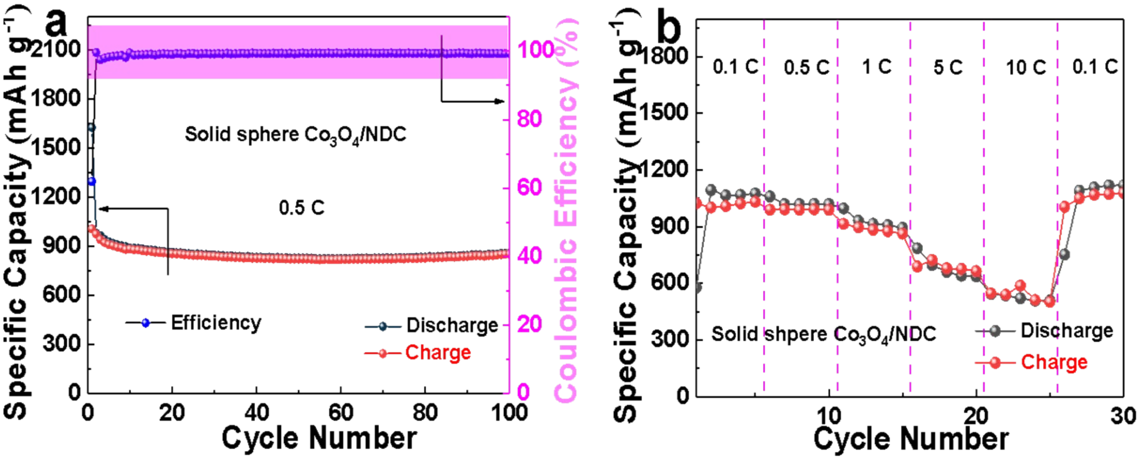

Fig. S25. Cycling performance and coulomb efficiency at current density of 0.5 C (a), rate performance (b) of solid sphere Co_3O_4/NDC.

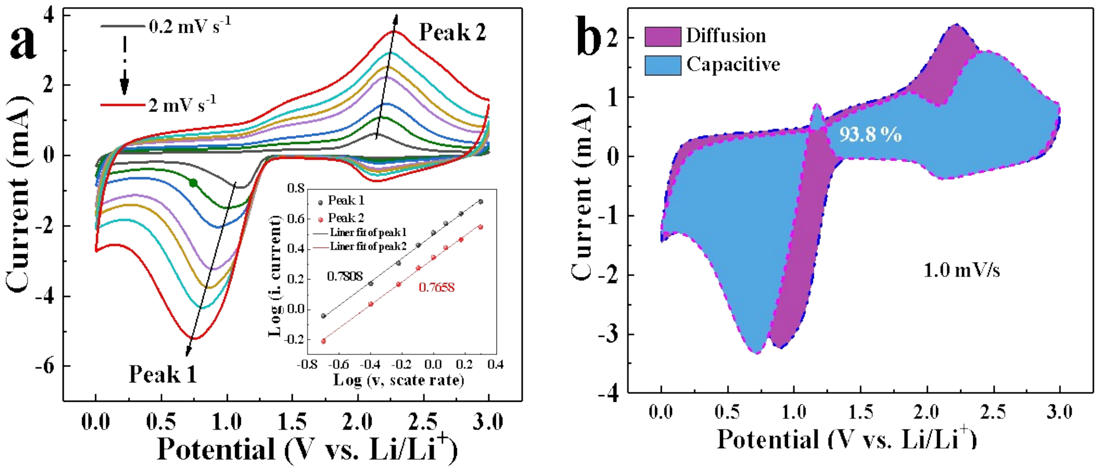

Fig. S26. Cyclic voltammetry (CV) curves (a) at different scan rates (Inset the relationship between peak current and scan rate linear), the capacitive charge and total charge at 1.0 mV s^{-1} (b) of open yolk-shell Co_3O_4/NDC.

A previous reports that the rate performance and cycle performance are influenced by surface capacitance behavior[21]. To quantitatively analyze the capacitive behavior of open yolk-shell Co_3O_4/NDC, its CV curves are measured at different scan rates (**Fig. S26a**). A power law is used to describe the relationship between the peak current (i) and the scan rate (v)[21, 22].

$$i = av^b \tag{S3}$$

When b=1, the material is controlled by the capacitive behavior. When b=0.5, then the diffusion controlled process is the main[23]. By plotting, the b values are calculated to be 0.7808 and 0.7658 for the cathode and anode peaks, respectively (**Fig. S26a**, inset part), indicating that there is not only capacitance behavior but also diffusion control. In order to accurately obtain the values of the capacitive contribution (k_1v) and diffusion contribution ($k_2v^{1/2}$), We use the following formula[23].

$$\mathrm{i} = \mathrm{k}_1\mathrm{v} + \mathrm{k}_2\mathrm{v}^{0.5} \tag{S4}$$

Therefore, the capacitive and diffusion contributions can be obtained. At a scan rate of 1 mV s^{-1}, the capacitive behavior of open yolk-shell Co_3O_4/NDC accounts for about 93.8% (**Fig. S26b**).

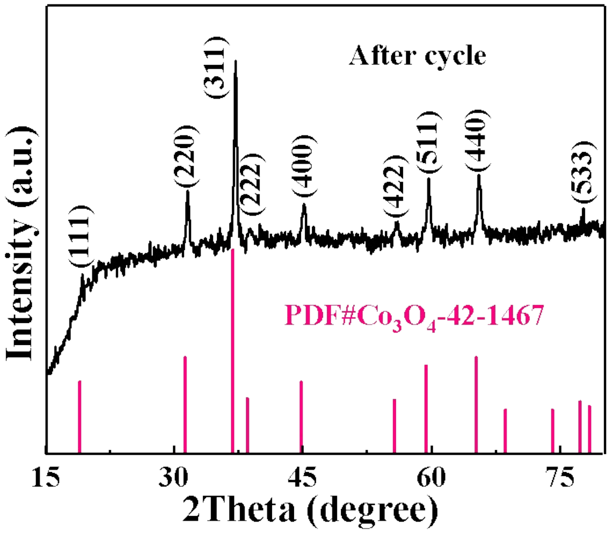

Fig. S27. XRD pattern of open yolk-shell Co_3O_4/NDC after 100 cycles at current density of 0.5 C.

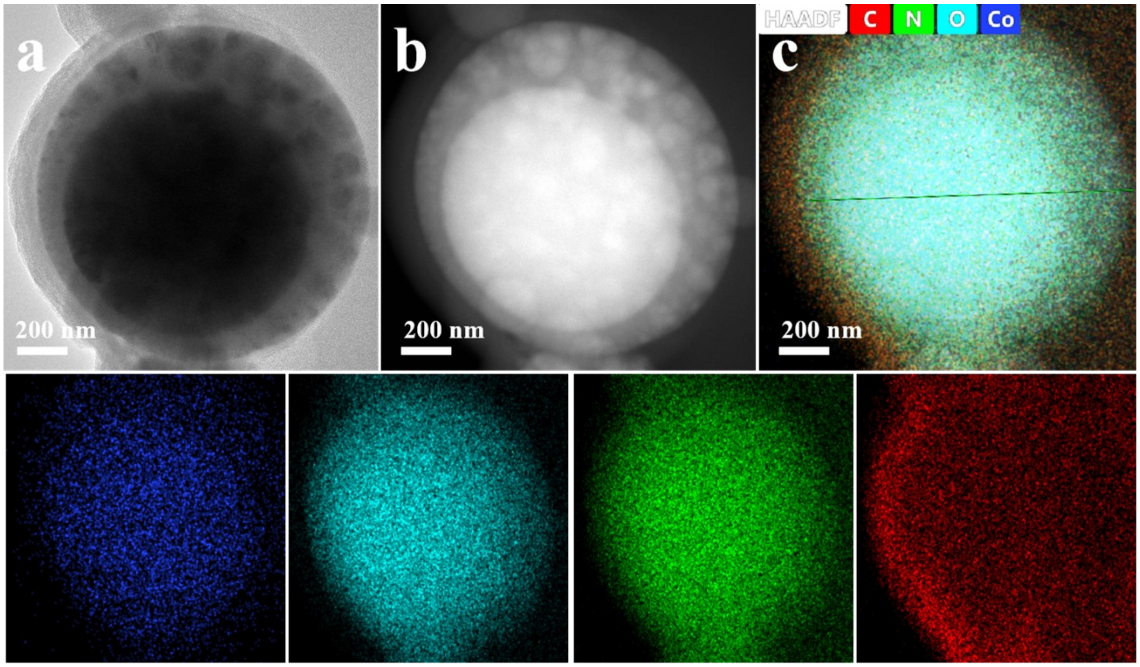

Fig. S28. TEM image (a), HAADF-STEM image (b) and element mapping (c) of open yolk-shell Co_3O_4/NDC after 100 cycles at current density of 0.5 C.

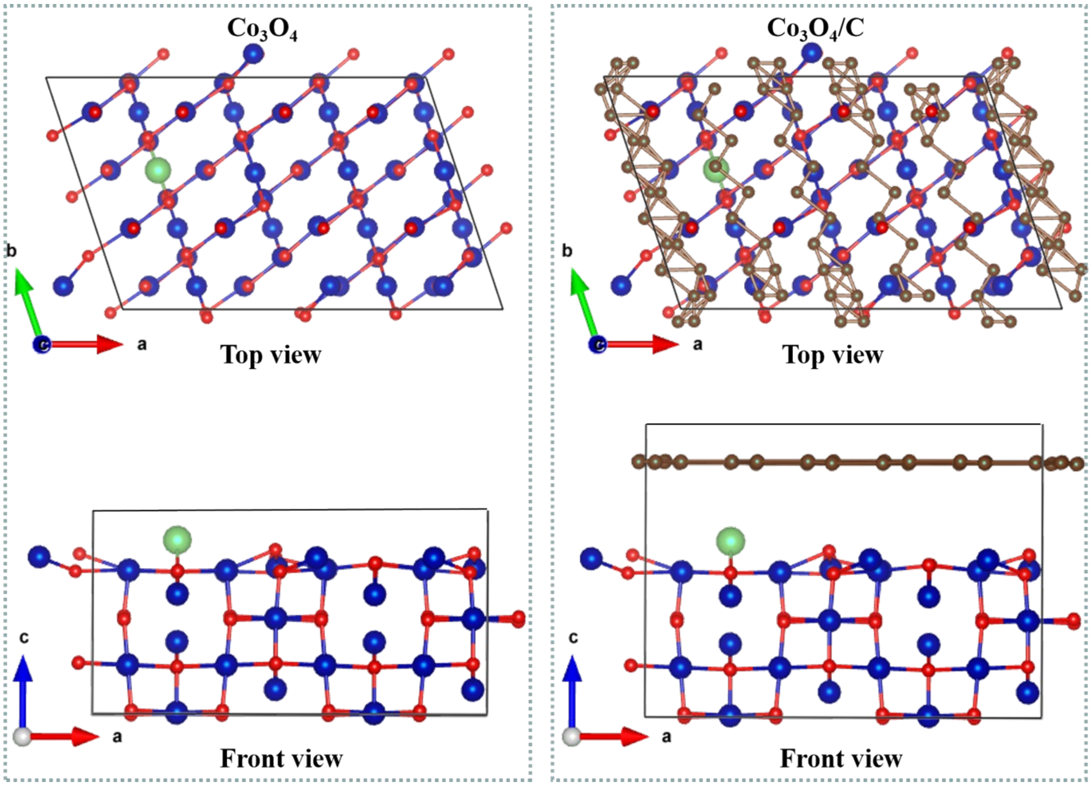

Fig. S29. The models of (a) Co_3O_4 super cell and (b) Co_3O_4/carbon.

Table S2. The full names and molecular structures of the three ILs are listed.

Full names	Molecular formula	Structure formula
1-butyl-3-methylimidazolium dicyanamide	$C_{10}H_{15}N_5$	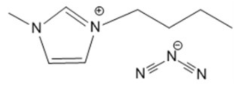
1-ethyl-3-methylimidazolium dicyanamide	$C_8H_{11}N_5$	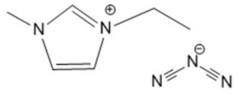
1-butyl-3-methylimidazolium tetrafuoroborate	$C_8H_{11}N_2BF_4$	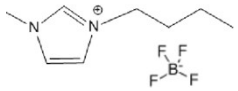

Table S3. Diffusion energy of lithium diffusion for the Co_3O_4/C and Co_3O_4 systems.

System	Diffusion energy (eV)			
Co_3O_4	0	4.58	1.24	0
Co_3O_4/C	0	0.76	0.59	0

Table S4. The electrochemical performance comparison of the Co_3O_4-based anode materials lately published for LIBs.

Materials	Method	Specific capacity	Rate performance	References
Co_3O_4 microspheres decorated by N-doped amorphous carbon shell	Air-injection in dopamine-tris solution and annealing	1074 mAh g^{-1} @ 500 mA g^{-1} after 500 cycles	830 mAh g^{-1} @ 1000 mA g^{-1}	[24]
Nitrogen-doped porous carbon spheres anchored with Co_3O_4	Hydrothermal method	984 mAh g^{-1} @ 100 mA g^{-1} after 100 cycles	659 mAh g^{-1} @ 5 A g^{-1}	[25]
Binder-Free Co_3O_4/Graphene sandwich-Like hybrid	Electrophoretic deposition	1113 mAh g^{-1} @ 0.2 A g^{-1} after 100 cycles	602 mAh g^{-1} @ 1 A g^{-1}	[26]
Nitrogen-rich MOF derived porous Co_3O_4/NDC	Chemical transformation of N-rich Co-MOF at 500 °C	612 mAh g^{-1} @ 1 A g^{-1} after 500 cycles	128 mAh g^{-1} @ 5 A g^{-1}	[27]
Carbon doped Co_3O_4 hollow nanofibers	Bifunctional polymeric nanofibers as template and carbon source	1121 mAh g^{-1} @ 0.2 A g^{-1} after 100 cycles	607 mAh g^{-1} @ 3 A g^{-1}	[28]
Mesoporous Co_3O_4 nanowires confi ned by N-Doped Graphene Aerogel	Hydrothermal reaction followed by calcination	1200 mAh g^{-1} @ 100 mA g^{-1} after 100 cycles	812 mAh g^{-1} @ 1 A g^{-1}	[29]
Co_3O_4/C nanocapsules with onion-like carbon shells	Modified arc-discharge method and 300 °C for 2 h in air	1027 mAh g^{-1} @ 0.5 C after 50 cycles	925 mAh g^{-1} @ 2 C	[30]
Co_3O_4-C core-shell nanowire array	Hydrothermal synthesis and direct current magnetron sputtering	989 mAh g^{-1} @ 0.5 C after 50 cycles	676 mAh g^{-1} @ 2 C	[31]
Hollow Co_3O_4 embedded in N,S dual doped reduced graphene oxide	Nanoscale Kirkendall effect	1605 mAh g^{-1} @ 200 mA g^{-1} after 150 cycles	1471 mAh g^{-1} @ 1 A g^{-1}	[32]
Co_3O_4 nanospheres embedded in	Hydrothermal reaction and 300 °C	1169 mAh g^{-1} @ 200	633 mAh g^{-1} @ 10 A	[33]

nitrogen doped carbon	for 8 h in air	mA g^{-1} after 100 cycles	g^{-1}	
Open yolk-shell Co_3O_4/NDC	Solvothermal method	1220 mAh g^{-1} @ 0.5 C after 100 cycles	584 mAh g^{-1} @ 5 C after 500 cycles	Our work

In-situ TEM videos

Two video clips were captured during the *in-situ* TEM measurement as video 1 and video 2. Video 1 shows that the amCoC microstructure of the yolk-shell gradually shrinks during the heating process from 25 ^{o}C to 360 ^{o}C. It can be seen that, as the temperature increases, the amCoC microstructure gradually shrinks along the edge. Video 2 shows that when the sample was held at 360 ^{o}C, the size of the amCoC microstructure remain unchanged, but the black spots on the surface of the amCoC gradually increased. To allow readers to observe the structural changes more clearly, both video clips have been speeded up for 3.5 times.

References

1. H. Jin, S. Xin, C. Chuang, W. Li, H. Wang, J. Zhu, H. Xie, T. Zhang, Y. Wan and Z. Qi, *Science*, 2020, **370**, 192-197.
2. K. Zhao, F. Liu, C. Niu, W. Xu, Y. Dong, L. Zhang, S. Xie, M. Yan, Q. Wei and D. Zhao, *Adv. Sci.,* 2015, **2**, 4443-4464.
3. T. Liu, F. Cao, L. Xiao, X. Li, S. Sun, X. Sun, Z. Zang, Q. Niu, J. Wu and J. Wu, *J. Electroanal. Chem.*, 2017, **807**, 52-58.
4. D. Adekoya, H. Chen, H. Y. Hoh, T. Gould and S. Zhang, *ACS Nano*, 2020, **14**, 5027-5035.
5. M. Shi, Z. Chen and J. Sun, *Cement & Concrete Research*, 1999, **29**, 1111-1115.
6. Y. Ma, P. Liu, Q. Xie, C. Zhang and D. L. Peng, *Mater. today energy,* 2020, **16**, 100383-100393.
7. Y. Liang, Y. Li, H. Wang, J. Zhou, J. Wang, T. Regier and H. Dai, *Nat. Mater.*, 2011, **10**, 780-786.

8. Y. H. Zhang, C. N. Wang, F. L. Gong, J. L. Chen, K. F. Xie, H. L. Zhang and S. M. Fang, *J. Mater. Chem. C,* 2021, **9**, 6078-6086.
9. B. H. Han, D. N. Qian, M. Risch, H. L. Chen and M. F. Chi, *J. Phys. Chem. Lett.,* **2015,** *8*, 1357-1362.
10. J. Gazquez, W. Luo, M. P. Oxley, M. Prange, M. A. Torija, M. Sharma, C. Leighton, S. T. Pantelides, S. J. Pennycook and M. Varela, *Nano Lett.*, 2011, **11**, 973-976.
11. X. Zhang, Z. Mao, Y. Zhao, Y. Wu and X. Wang, *J. Mater. Sci.,* 2020, **55**, 5445-5457.
12. H. Wang, X. B. Li, L. Gao, H. L. Wu, J. Yang, L. Cai, T. B. Ma, C. H. Tung, L. Z. Wu and G. Yu, *Angew. Chem., Int. Ed.,* 2017, **57**, 192-197.
13. M. Xiao, Y. Meng, Y. Li, X. Liu and F. Zhu, *Appl. Surf. Sci.,* 2019, **494**, 532-539.
14. Z. M. C. Lu, *Carbon*, 2011, **25**, 475-478.
15. M. E. Davis, *Nature*, 2010, **33**, 245-245.
16. S. Zafeiratos, T. Dintzer, D. Teschner, R. Blume, M. HäVecker, A. Knop-Gericke and R. SchlöGl, *J. Catal.*, 2010, **269**, 309-317.
17. T. Sharifi, G. Hu, X. Jia and T. Wågberg, *ACS Nano*, 2012, **6**, 8904-8912.
18. L. Feng, Y. Yan, Y. Chen and L. Wang, *Energy Environ. Sci.*, 2011, **4**, 1892-1899.
19. V. M. Dhavale, S. S. Gaikwad and S. Kurungot, *J. Mater. Chem. A,* 2013, **2**, 1383-1390.
20. L. Feng, Y. Yan, Y. Chen and L. Wang, *Energy Environ. Sci.,* 2011, **4**, 1892-1899.
21. Q. Long, W. M. Chen, Z. H. Wang, Q. G. Shao, X. Li, L. X. Yuan, X. L. Hu, W. X. Zhang and Y. H. Huang, *Adv. Mater.*, 2012, **24**, 2047-2050.
22. S. Lu, T. Zhu, Z. Li, Y. Pang, L. Shi, S. Ding and G. Gao, *J. Mater. Chem. A*, 2018, **6**, 7005-7013.
23. Z. Hu, L. Wang, K. Zhang, J. Wang, F. Cheng, Z. Tao and J. Chen, *Angew. Chem., Int. Ed.,* 2014, **53**, 12794-12798.

24. M. Liu, X. Hou, T. Wang, Y. Ma, K. Sun, D. Liu, Y. Wang, D. He and J. Li, *Electrochim. Acta*, 2018, **283**, 979-986.

25. Y. Ding, C. Qin, W. Li, J. Du, Z. Fu, W. Song and F. Wang, *Electrochim. Acta*, 2016, **187**, 234-242.

26. Y. Yang, J. Huang, J. Zeng, J. Xiong and J. Zhao, *ACS Appl. Mater. Interfaces*, 2017, **9**, 32801-32811.

27. X. Han, W. M. Chen, X. Han, Y. Z. Tan and D. Sun, *J. Mater. Chem. A*, 2016, **4**, 13040-13045.

28. C. Yan, G. Chen, X. Zhou, J. Sun and C. Lv, *Adv. Funct. Mater.*, 2016, **26**, 1428-1436.

29. X. Yao, G. Guo, Y. Zhao, Y. Zhang and Y. Zhao, *Small*, 2016, **12**, 3849-3860.

30. X. Liu, S. W. Or, C. Jin, Y. Lv, W. Li, C. Feng, F. Xiao and Y. Sun, *Electrochim. Acta*, 2013, **100**, 140-146.

31. J. Chen, X. H. Xia, J. P. Tu, Q. Q. Xiong, Y. X. Yu, X. L. Wang and C. D. Gu, *J. Mater. Chem.*, 2012, **22**, 15056-15061.

32. J. Zhu, W. Tu, H. Pan, H. Zhang, B. Liu, Y. Cheng, Z. Deng and H. Zhang, *ACS Nano*, 2020, **14**, 5780-5787.

33. H. H. Li, L. Zhou, L. L. Zhang, C. Y. Fan, H. H. Fan, X. L. Wu, H. Z. Sun and J. P. Zhang, *ACS Energy Lett.,* 2016, **2**, 52-59.